An ENDOR study of RbI:O_2^-

1995 J. Phys.: Condens. Matter 7 1909

(http://iopscience.iop.org/0953-8984/7/9/015)

J. Phys.: Condens. Matter 7 (1995) 1909–1919. Printed in the UK

An ENDOR study of RbI:O_2^-

S Van Doorslaer†, F Callens‡, F Maes and P Matthys

Laboratory for Crystallography and Study of the Solid State, Krijgslaan 281-S1, B-9000 Gent, Belgium

Received 8 November 1994, in final form 7 December 1994

Abstract. In this work, an ENDOR analysis of the O_2^- defect in RbI is presented. A complete angular variation of one set of ^{85}Rb and ^{87}Rb ENDOR transitions is shown. The corresponding hyperfine and nuclear quadrupole coupling tensors are determined. The orientation of the principal axes of these tensors is in good agreement with the overall D_{2h} symmetry of the O_2^- ion in the crystal. The ENDOR results can only be explained assuming a monovacancy model, wherein the O_2^- molecule is replacing a single I^- ion. A comparison with a previous ENDOR study of the S_2^- centre in RbCl is presented. The linewidth of the EPR signals can be explained using the ENDOR results.

1. Introduction

In the past several EPR studies have been performed on X_2^- defects (X=O, S or Se) in alkali halide single crystals [1–12]. Although interesting features emerged from these EPR studies, it was sometimes difficult to determine unambiguously the total defect structure. Problems arose when in KCl two different S_2^- molecular ions were identified in the same single-crystal sample. From the work of the groups of Känzig [1–3] and Vannotti [4,5] and our EPR group [6–12], it is known that, depending on the lattice, the paramagnetic p lobes of the X_2^- defect may be oriented along a [$\bar{1}$10] or a [001] direction. Because in the KCl:S_2^- case both situations were found, the monovacancy model for some X_2^- defects was questioned and a divacancy model (in which X_2^- is replacing two halide ions) was also considered.

Since the ENDOR method is more suited to solve such problems, ENDOR investigations on a whole series of X_2^- defects (X=O, S and Se) in different alkali halide crystals were started. The ENDOR study of RbCl:S_2^- [13] clearly led to a monovacancy model. However, the ENDOR features of the S_2^- defect in NaCl and NaBr turned out to be very different from those of the Se_2^- defects in the same single crystals and neither of them could be related to the RbCl:S_2^- case (these ENDOR results will be discussed in later papers). In order to elucidate this matter, ENDOR studies on O_2^- defects in alkali halide single crystals were started. Based on their EPR results, Zeller and Känzig [2] proposed a monovacancy model for these defects. Since the O_2^- molecule is much smaller than the S_2^- and Se_2^- molecules, the O_2^- molecule is indeed likely to fit into a monovacancy in the alkali halide single crystals.

In this article, we report on the ENDOR study of the O_2^- centre in RbI.

† Research assistant of the NFSR, Belgium.

‡ Senior research associate of the NFSR, Belgium.

0953-8984/95/091909+11$19.50

2. Experimental techniques

The single crystals were grown by the Bridgman method. The RbI powder (Merck) was mixed up with 1% KO_2 (Merck). Samples thus grown were routinely quenched from 600 °C to room temperature (RT), though this treatment did not affect the O_2^- spectra reported below. The crystals were x-irradiated at RT for typically $\frac{1}{2}$ h with a tungsten anticathode Philips x-ray tube, operated at 60 kV and 40 mA.

The EPR spectra were recorded using a Bruker ESP 300 X band spectrometer, with maximum microwave power 200 mW. The detection conditions were 10 K and 10 mW microwave power.

The ENDOR spectra were recorded on the same spectrometer, equipped with a Bruker ESP 353E ENDOR/triple extension (an EN 374 RF amplifier with a maximum power of 200 W and an EN 525 Schomandl synthesizer). The best detection conditions were 7.5 K and 30 mW microwave power at maximum RF power. The RF was modulated at 12.5 kHz with a modulation depth of 100 kHz.

3. Results and analysis

3.1. EPR spectra

The EPR spectra of RbI:O_2^- were studied by Zeller and Känzig [2]. The **g** tensor values of this orthorhombic centre are found to be $g_x = 1.9674$, $g_y = 1.9695$ and $g_z = 2.3774$, with corresponding axes parallel to $[\bar{1}10]$, [001] and [110]. Shuey and Zeller [3] showed that this implies that the paramagnetic p lobes correspond to the x direction (the smallest g value) and that the largest g value is found along the O–O axis (the z direction). The linewidth of the EPR signals was ascribed to an unresolved superhyperfine (SHF) structure.

3.2. ENDOR spectra

3.2.1. General remarks. In the ENDOR spectra transitions belonging to ^{85}Rb, ^{87}Rb and ^{127}I are found. The Rb interaction is labelled interaction 1, in agreement with the Rb interaction 1 observed in RbCl:S_2^- [13].

3.2.2. ENDOR spectra corresponding to Rb interaction 1. The ENDOR angular variations for the Rb SHF interaction (both isotopes) are measured in the g_x–g_z plane (plane 1, $\boldsymbol{B}_0 \perp [001]$) and in the plane containing the g_y axis ($\boldsymbol{B}_0 \perp [100]$ or $\boldsymbol{B}_0 \perp [010]$). This plane is called plane 2. Since we are technically limited to detecting ENDOR transitions above 0.8 MHz, some lines of the ^{85}Rb angular variation are missing. For both isotopes, the low-frequency lines were found to be less intense than those corresponding to the other manifold.

In figure 1, the angular variations for both Rb isotopes are given. Figure 2 shows a typical ENDOR spectrum.

The spectra were analysed using the standard Hamiltonian for a single nucleus ($I > \frac{1}{2}$) coupled with an unpaired electron ($S = \frac{1}{2}$)

$$\hat{H} = \beta \hat{S}^{\mathrm{T}} \mathbf{g} B + \hat{I}^{\mathrm{T}} \mathbf{A} \hat{S} - \beta_{\mathrm{N}} \hat{I} \mathbf{g}_{\mathrm{N}} B + \hat{I}^{\mathrm{T}} \mathbf{Q} \hat{I}. \tag{1}$$

The ENDOR frequencies were analysed by complete diagonalization of the spin Hamiltonian matrix. The resulting principal values and corresponding axes of the hyperfine tensor and nuclear quadrupole tensor are given in table 1.

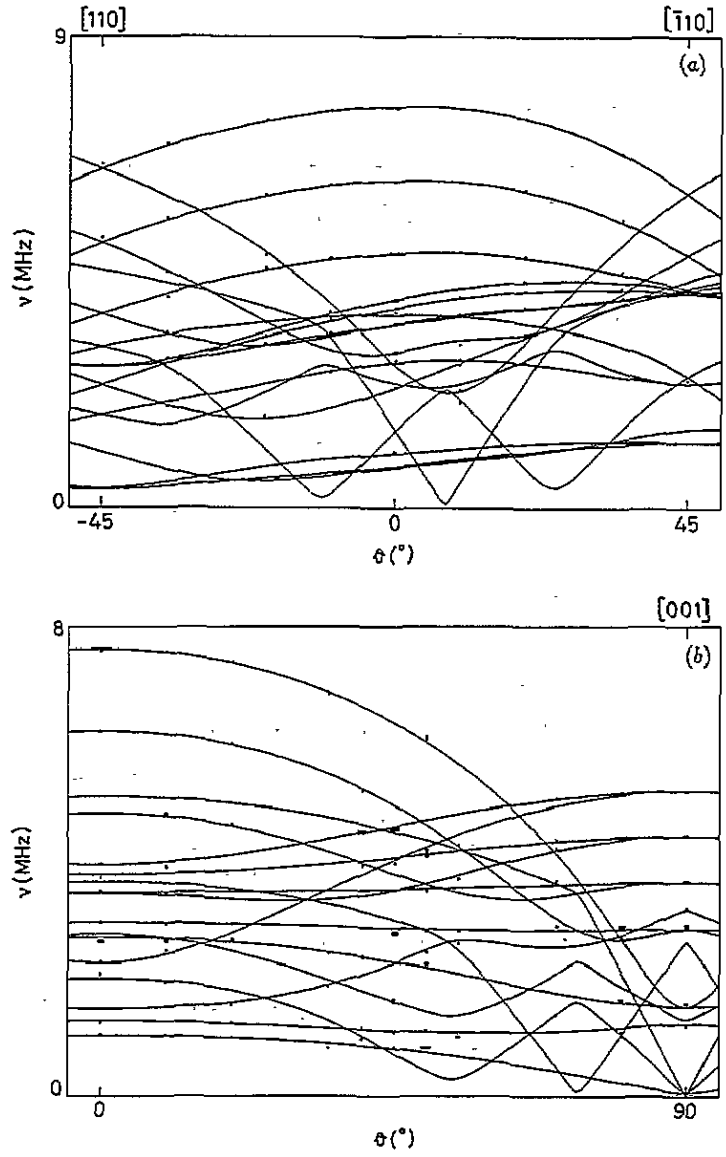

Figure 1. For interaction 1: (*a*) ^{85}Rb angular variation in plane 1; (*b*) ^{85}Rb angular variation in plane 2; (*c*) ^{87}Rb angular variation in plane 1; (*d*) ^{87}Rb angular variation in plane 2. Rectangles, experimental points; lines, theoretical angular variation calculated using the values of table 1. (Continued overleaf.)

The theoretical angular variations, calculated using the values of table 1, are shown in figure 1 (full lines).

From table 1, we see that the **A** tensor is nearly axial ($|A_y| \approx |A_z| < |A_x|$). No information about the absolute sign can be obtained from ENDOR experiments. Nevertheless, we are very confident about the positive signs, because of the correspondence with Rb interaction 1 found in RbCl:S_2^- [13]. Two principal axes of the **A** tensor are tilted away from the g_x and g_z axes in the (001) plane. The **Q** tensor is found to be rhombic, with the axis corresponding to the largest Q value ($|Q_x|$) tilted 55.4° away from the g_x axis.

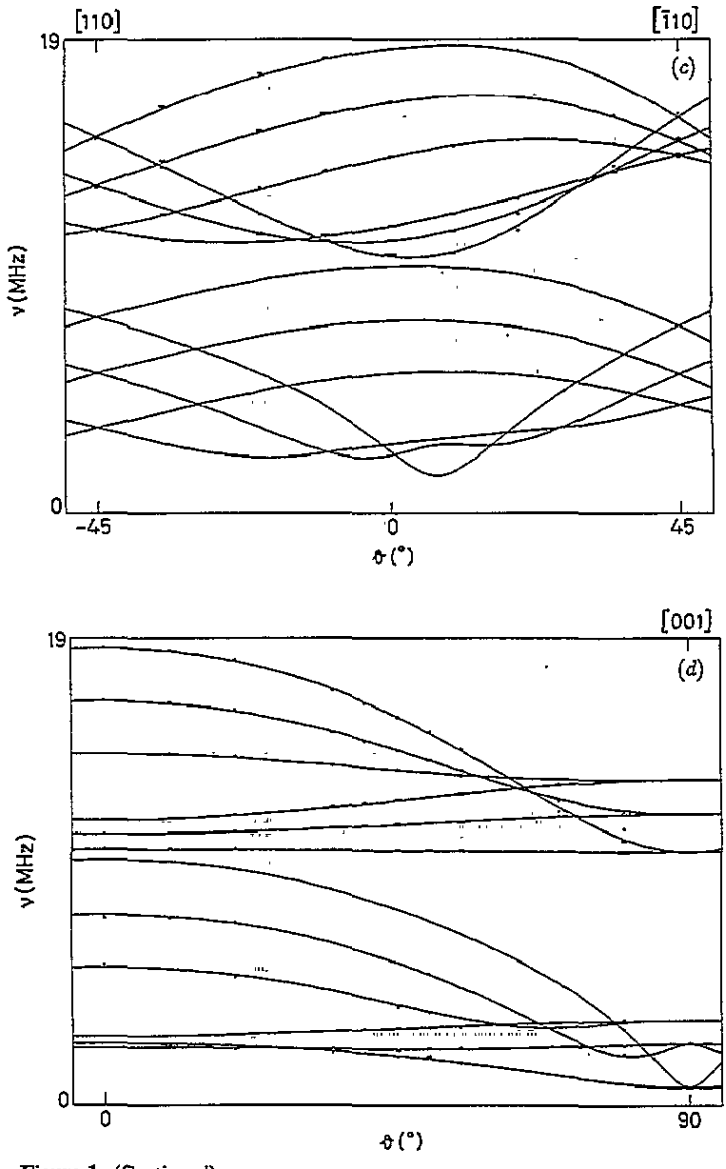

Figure 1. (Continued)

3.2.3. Other ENDOR transitions. In the 0–5 MHz region, three ENDOR lines were found, which correspond to the ^{85}Rb, ^{87}Rb and ^{127}I ν_N signals. These signals are caused by Rb, or I nuclei at a relatively large distance from the O_2^- defect. Since the linewidth of the ENDOR lines is about 100 kHz, the Rb and I nuclei giving rise to the ν_N signals are located at least 0.8 nm and 0.7 nm from the O_2^- defect respectively.

4. Discussion

Until now, the location of the Rb nuclei causing interaction 1 has not been commented on. From the EPR results, Zeller and Känzig [2] assumed that the O_2^- molecule occupied

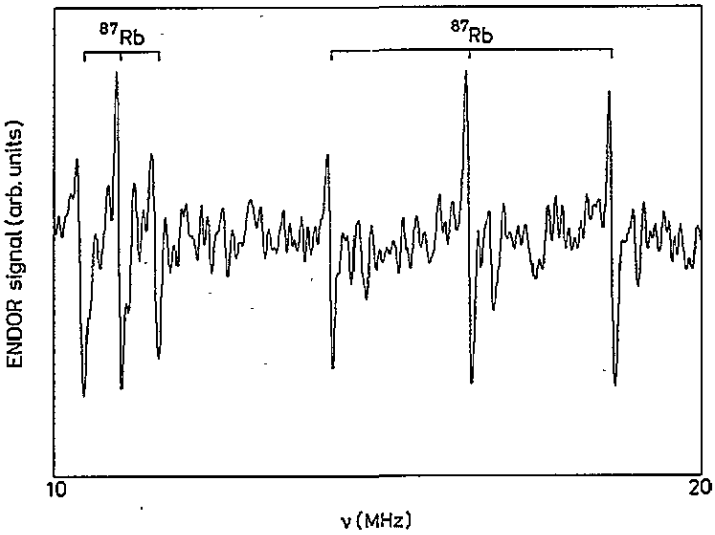

Figure 2. The experimental ^{87}Rb ENDOR spectrum of RbI:O_2^- (only the upper manifold is shown), $B_0 \parallel [100]$, $T = 7.5$ K, 200 W RF power and 100 kHz modulation depth.

Table 1. Principal values (in megahertz) and axes (angles in degrees) of the ^{85}Rb and ^{87}Rb SHF and nuclear quadrupole tensors for interaction 1.

			Angles with respect to		
	^{85}Rb	^{87}Rb	g_x	g_y	g_z
A_x	7.22	24.46	−40.0	90	50.0
A_y	4.07	13.80	90	0	90
A_z	3.88	13.16	−130.0	90	−40.0
Q_x	0.48	0.75	−55.4	90	34.6
Q_y	−0.31	−0.49	90	0	90
Q_z	−0.17	−0.26	−145.4	90	−55.4

a monovacancy, replacing a single I^- ion (figure 3). In what follows, we will confirm their assumption and give additional information that could not be determined using EPR. Rb interaction 1 will be shown to be due to the nearest-neighbour Rb nuclei in the g_x–g_z plane (figure 3, A1). Furthermore, we will compare our present results with those obtained previously for RbCl:S_2^- [13].

4.1. The superhyperfine tensor

Zeller and Känzig [2] showed that the ground state of the centre can be described as follows:

$$|\Psi\pm\rangle = \cos\alpha|\Gamma_2^+\rangle|\pm\tfrac{1}{2}\rangle \pm i\sin\alpha|\Gamma_4^+\rangle|\pm\tfrac{1}{2}\rangle \pm (\lambda/2E)(\cos\alpha - \sin\alpha)|\Gamma_1^+\rangle|\mp\tfrac{1}{2}\rangle \qquad (2)$$

with $\tan(2\alpha) = \lambda/\Delta$ and $|\pm\frac{1}{2}\rangle$ the eigenstates of $\hat{S}_z$. Γ_1^+, Γ_2^+ and Γ_4^+ are irreducible representations of the D_{2h} symmetry group [14]. In (2), Δ and E are crystal field parameters and λ is the positive spin–orbit coupling constant. For the RbI:O_2^- case, Zeller and Känzig [2] found that $\lambda/\Delta = 0.1898$, $\lambda/E = 0.0013$, $\cos\alpha = 0.9956$ and $\sin\alpha = 0.0937$. The

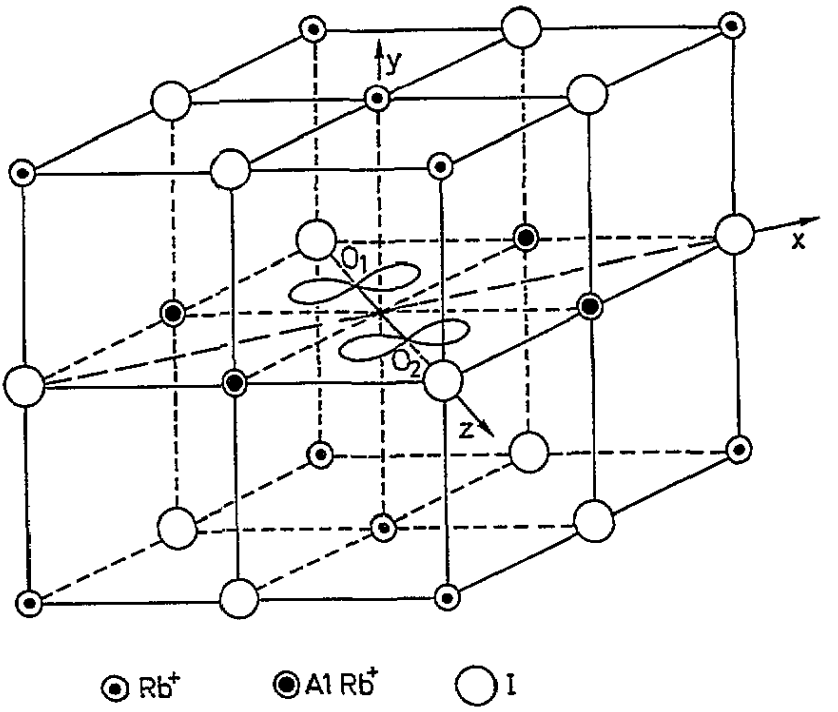

Figure 3. The monovacancy model of O_2^- in RbI. The Rb^+ ions labelled A1 are responsible for interaction 1.

$|\Gamma_2^+\rangle$ state clearly contributes the most to the ground state of the paramagnetic centre. In the $|\Gamma_2^+\rangle$ state the unpaired electron resides in a molecular orbital of the form $(p_{x1} - p_{x2})/\sqrt{2}$, where 1 and 2 denote the different oxygen atoms (figures 3 and 4).

To calculate the SHF components of the nearest-neighbouring cations, we have to consider both point dipolar contributions and covalency effects.

The point dipolar contribution in a system with anisotropic **g** tensor is given by the following expression [15]:

$$A_{ij}^{d} = (\mu_0/4\pi)(\alpha_N/r^3)g_j(3r_ir_j - \delta_{ij}) \qquad (i, j = x, y, z) \tag{3}$$

with

$$\alpha_N = \beta\beta_N g_N/h$$

and

$$r_x = \cos\phi_N \sin\theta_N \qquad r_y = \sin\phi_N \sin\theta_N \qquad r_z = \cos\theta_N$$

the direction cosines of the nucleus in the **g** tensor axes.

To include covalency effects, the expressions for the SHF components of the four Rb nuclei A1 (figure 4) derived by Shuey and Zeller [3] are used.

For the unpaired electron in the neighbourhood of the alkali nuclei, the following wavefunction is considered for Rb nucleus 1:

$$|\Psi\pm\rangle \approx \cos\alpha(c_\sigma\phi_\sigma + c_s\phi_s)|\pm\tfrac{1}{2}\rangle \pm i\sin\alpha c_\pi\phi_\pi|\pm\tfrac{1}{2}\rangle \tag{4}$$

where

$$\phi_\sigma = -(4p)_x \cos\delta + (4p)_z \sin\delta \qquad \phi_\pi = (4p)_y \qquad \phi_s = (4s) \tag{5}$$

and δ is the angle between the g_x axis and the ϕ_σ lobe. To a first approximation, the ϕ_σ lobe is taken to be along the axis connecting the Rb nucleus and the nearest O nucleus. The O–O distance and the Rb–I distance along a ⟨100⟩ axis are taken to be 0.128 nm [16] and 0.368 nm respectively, which leads to a value for δ of 37.0°.

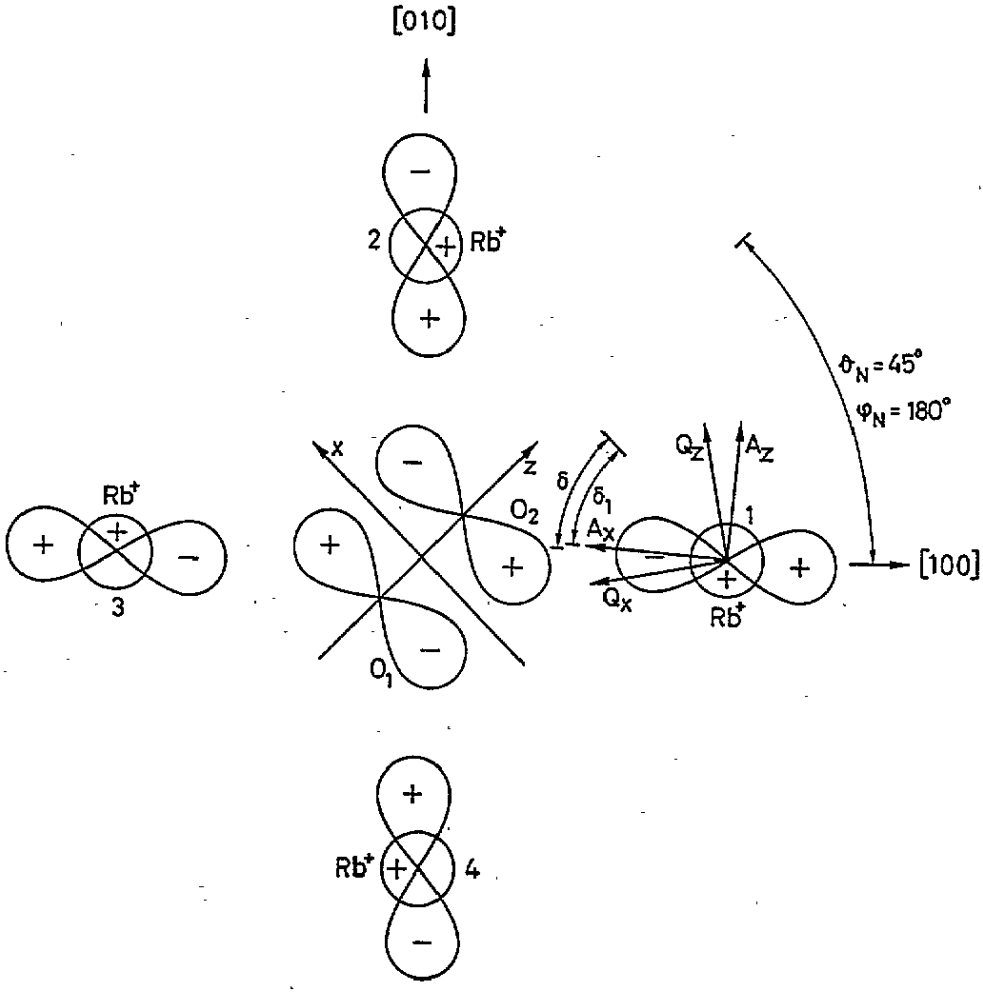

Figure 4. The orientation of the principal axes of the Rb SHF and nuclear quadrupole tensors. δ is the angle between the g_x axis and the ϕ_σ lobe; δ_1 is the angle between the A_x axis and the g_x axis.

Using (4) the following components of the SHF matrix result:

$$
\begin{aligned}
A^{c}_{yy} &= A_s - \tfrac{2}{3}A_\sigma - A_\pi \cos\delta \\
A^{c}_{xx} &= A_s + A_\sigma(\tfrac{1}{3} + \cos 2\delta) + A_\pi \cos\delta \\
A^{c}_{zz} &= A_s + A_\sigma(\tfrac{1}{3} - \cos 2\delta) - \tfrac{10}{3}A_\pi \cos\delta \\
A^{c}_{zx} &= -A_\sigma \sin 2\delta - A_\pi \sin\delta \\
A^{c}_{xz} &= -A_\sigma \sin 2\delta - \tfrac{10}{3}A_\pi \sin\delta
\end{aligned} \tag{6}
$$

in which the superscript c denotes covalency and A_s, A_σ and A_π (in megahertz) are defined as follows:

$$
\begin{aligned}
A_s &= \cos^2\alpha c_s^2 (8\pi/3)|\Psi(0)|^2_{alk}((\mu_0/4\pi)g_N g_e \beta\beta_N \times 10^{-6}/h) \\
A_\sigma &= \cos^2\alpha c_\sigma^2 \tfrac{3}{5}\langle 1/r^3\rangle_{alk}((\mu_0/4\pi)g_N g_e \beta\beta_N \times 10^{-6}/h) \\
A_\pi &= \sin 2\alpha c_\sigma c_\pi \tfrac{3}{5}\langle 1/r^3\rangle_{alk}((\mu_0/4\pi)g_N g_e \beta\beta_N \times 10^{-6}/h).
\end{aligned} \tag{7}
$$

By adding the matrix elements A^{d}_{ij} of (3) (with $\theta_N = 45°$ and $\phi_N = 180°$ (see figure 4)) and the corresponding elements A^{c}_{ij} of (6), we obtain an asymmetric **A** matrix. The symmetric tensor $\mathbf{A}^T\mathbf{A}$ can easily be diagonalized and should be compared to the experimentally obtained data in the following way:

$$
\begin{bmatrix} \cos\delta_1 & 0 & -\sin\delta_1 \\ 0 & 1 & 0 \\ \sin\delta_1 & 0 & \cos\delta_1 \end{bmatrix}
\begin{bmatrix} A_{xx} & 0 & A_{zx} \\ 0 & A_{yy} & 0 \\ A_{xz} & 0 & A_{zz} \end{bmatrix}
\begin{bmatrix} A_{xx} & 0 & A_{xz} \\ 0 & A_{yy} & 0 \\ A_{zx} & 0 & A_{zz} \end{bmatrix}
\begin{bmatrix} \cos\delta_1 & 0 & \sin\delta_1 \\ 0 & 1 & 0 \\ -\sin\delta_1 & 0 & \cos\delta_1 \end{bmatrix}
$$
$$
= \begin{bmatrix} (7.24\ \text{MHz})^2 & 0 & 0 \\ 0 & (4.04\ \text{MHz})^2 & 0 \\ 0 & 0 & (3.90\ \text{MHz})^2 \end{bmatrix} \tag{8}
$$

where δ_1 corresponds with the experimentally found tilt angle between the A_x and g_x axis (40°) (see figure 4).

Combining (3), (6), (7) and (8), we were able to find values for r, A_s, A_π and A_σ. With $\delta = 37.0°$, it was not possible to fit the hyperfine values exactly. However, when varying δ, we found that for $\delta = 41.6°$, we could perfectly fit the theory to the experiment. The change in δ is not unexpected, since we only took ϕ_σ to be along the Rb–O direction in a first approximation. The values thus obtained for the coefficients c_s^2, c_π^2 and c_σ^2 are given in table 2. The distance r between the Rb nucleus and the centre of the O_2^- molecule is found to be 0.368 nm, which is also the lattice constant of RbI.

Table 2. A comparison between the calculated coefficients c_s^2, c_π^2 and c_σ^2 obtained from the ENDOR results for RbI:O_2^- (a) and RbCl:S_2^- (b), taking into account that $|\Psi(O)|^2_{4s} = 29.28 \times 10^{25}$ cm^{-3} and $\langle r^{-3}\rangle_{4p} = 20.24 \times 10^{25}$ cm^{-3} [17].

	c_s^2	c_σ^2	c_π^2	$c_\pi c_\sigma$
(a)	0.000 409	0.002 02	0.000 378	0.000 874
(b)	0.002 140	0.009 79	0.000 590	0.002 410

Table 2 shows that the values of the coefficients in the RbI:O_2^- case are about five times smaller than for the RbCl:S_2^- case. Since the lattice constant is larger for RbI than for

RbCl and since the O_2^- molecule is smaller than the S_2^- molecule, the Rb σ (π) orbitals will overlap less with the O_2^- Γ_2^+ (Γ_4^+) orbitals than with the corresponding ones of the S_2^- molecule.

The magnetic point dipolar tensor is derived from (3). The diagonal elements are then $A_x^d = 0.34$ MHz, $A_y^d = -0.15$ MHz and $A_z^d = -0.16$ MHz. The axis corresponding to the largest value is tilted 38° away from the g_x axis. The inclusion of the anisotropic **g** tensor in (3) causes the principal axes to differ from the crystal axes.

Zeller and Känzig [2] ascribed the linewidth of the EPR signals to an unresolved SHF structure. If this is the case, the linewidth of the EPR lines must be predictable from the ENDOR results. Indeed, up to first order, the values of the SHF splitting K in the EPR spectra can be related to the SHF matrix elements A_{ij} obtained from the ENDOR analysis [18]. For the B_0 field parallel to the **g** tensor axes, we find

$$\begin{aligned} B_0 \| g_x &: K(10^{-4}\ \mathrm{T}) = \sqrt{A_{xx}^2 + A_{zx}^2}/\beta g_x \\ B_0 \| g_y &: K(10^{-4}\ \mathrm{T}) = A_{yy}/\beta g_y \\ B_0 \| g_z &: K(10^{-4}\ \mathrm{T}) = \sqrt{A_{zz}^2 + A_{xz}^2}/\beta g_z \end{aligned} \tag{9}$$

in which the **A** matrix elements are given in megahertz.

The values of the ^{85}Rb and ^{87}Rb splittings for these specific directions of the magnetic field are given in table 3.

Table 3. ^{85}Rb SHF splittings K (in 10^{-4} T) for some specific directions of the magnetic field, calculated using the ENDOR results.

$B_0\|$	^{85}Rb	^{87}Rb
[$\bar{1}$10]	2.20	7.46
[001]	1.48	5.01
[110]	1.66	5.63

The simulation of the resulting EPR line is complicated by the presence of both isotopes with differing natural abundance and the fact that four equivalent Rb ions contribute to the observed interaction. Assuming that each SHF line has a homogeneous linewidth of about 5×10^{-4} T, we could simulate the resulting EPR signals with unresolved SHF structure. The EPR linewidths are given in table 4 and compared with the ones found experimentally by Zeller and Känzig [2].

Table 4. A comparison between the EPR linewidths (in 10^{-4} T) obtained from the ENDOR results (a) and those obtained experimentally by Zeller and Känzig [2] (b).

$B_0\|$	ΔB (a)	ΔB (b)
[$\bar{1}$10]	21.0	20.5
[001]	15.3	15.2
[110]	16.8	18.6

It is clear that the observed linewidths of the EPR lines are due to the SHF interaction with the four nearest-neighbour Rb nuclei.

4.2. The nuclear quadrupole tensor

As a rule of thumb, the **Q** tensor should always have the same symmetry as the **A** tensor. This is the case for the interaction observed above.

However, the **Q** tensor axes are not parallel to the **A** tensor axes as was approximately the case for the S_2^- defect in RbCl. The difference in the tilt angles can be explained in the following way.

The calculation of the nuclear quadrupole tensor involves the determination of the field gradient. The elements of the field gradient tensor [19] are

$$V_{\alpha\beta} = (e/4\pi\varepsilon_0)\partial^2(1/r)/(\partial\alpha\,\partial\beta) \qquad (\alpha, \beta = x, y, z). \tag{10}$$

In a point approximation (i.e. the defect is approximated by an electron centred on a lattice position), the principal axes of the field gradient tensor are oriented along the [100], [010] and [001] axes. Secondly, if $I > \frac{1}{2}$, the nucleus has a non-spherical charge distribution. Combination of these two features implies that, at the nearest-neighbouring cation sites, the **Q** tensor will be axial with its symmetry axis in the radial direction of the defect (i.e. along a ⟨100⟩ axis).

For an electron in an atom or molecule, however, (10) must be integrated over the wavefunction. For atomic orbitals the calculation parallels that of the magnetic dipolar coupling. The field gradient is equal to zero for an s electron, while for p, d, ... electrons the tensor is uniaxial and traceless. For a many-electron system, a summation over all electrons should be considered.

For our specific case, the axial symmetry is broken because of this summation. Moreover, such an anisotropic effect also gives rise to a tilt of the **Q** tensor axes, so that one of the axes is no longer pointing towards the middle of the O_2^- centre. A similar effect was observed for the magnetic point dipolar coupling tensor, as mentioned earlier.

5. Conclusion

The ENDOR spectra of RbI:O_2^- allowed a detailed analysis of one set of ^{85}Rb and ^{87}Rb interactions. The orientations of the principal axes of the **A** and **Q** tensor of this interaction are in agreement with the overall D_{2h} symmetry of the O_2^- ion in the crystal.

The Rb interaction could be ascribed to the nearest-neighbour Rb ions in the (001) plane. Many similarities were found with an earlier ENDOR study of the S_2^- ion in RbCl [13]. Some information about the wavefunction of the unpaired electron in the neighbourhood of these Rb nuclei could be derived. Finally, the linewidth of the EPR signals could be explained from the ENDOR data.

The only model consistent with these ENDOR data is the one in which the O_2^- molecular ion is substituting for one I^- ion.

Acknowledgment

This work is part of a project sponsored by Interuniversitair Instituut voor Kernwetenschappen (IIKW), Belgium.

References

[1] Känzig W and Cohen M H 1959 *Phys. Rev. Lett.* **3** 509
[2] Zeller H R and Känzig W 1967 *Helv. Phys. Acta* **40** 845
[3] Shuey R T and Zeller H R 1967 *Helv. Phys. Acta* **40** 873
[4] Vannotti L E and Morton J R 1967 *Phys. Rev.* **161** 282
[5] Vannotti L E and Morton J R 1967 *Phys. Lett.* **24A** 250
[6] Matthys P, Callens F and Boesman E 1983 *Solid State Commun.* **45** 1
[7] Callens R, Callens F, Matthys P and Boesman E 1988 *Phys. Status Solidi* b **148** 683
[8] Callens F, Maes F, Matthys P and Boesman E 1989 *J. Phys.: Condens. Matter* **1** 6912
[9] Maes F, Callens F, Matthys P and Boesman E 1990 *J. Phys. Chem. Solids* **51** 1289
[10] Maes F, Callens F, Matthys P and Boesman E 1990 *Phys. Status Solidi* b **161** K1
[11] Maes F, Matthys P, Callens F and Boesman E 1991 *Solid State Commun.* **80** 583
[12] Maes F, Matthys P, Callens F, Moens P and Boesman E 1992 *J. Phys.: Condens. Matter* **4** 249
[13] Van Doorslaer S, Maes F, Callens F, Moens P and Boesman E 1994 *J. Chem. Soc. Faraday Trans.* **90** 2541
[14] Koster G F, Dimack J O, Wheeler R G and Statz H 1963 *Properties of the Thirty-Two Point Groups* (Cambridge, MA: MIT Press)
[15] Hurst G C, Henderson T A and Kreilick R W 1985 *J. Am. Chem. Soc.* **107** 7294
[16] Sutton L E (ed) 1958 *Tables of Interatomic Distances and Configurations in Molecules and Ions* (London: The Chemical Society) p M69
[17] Koh A K and Miller D J 1985 *At. Data Nucl. Data Table* **33** 235
[18] Iwasaki M 1974 *J. Magn. Reson.* **16** 417
[19] Atherton N M 1993 *Principles of Electron Spin Resonance* (Chichester: Ellis Horwood) pp 278–9